

BLOCK PRECONDITIONING TECHNIQUES FOR GEOPHYSICAL ELECTROMAGNETICS*

H. BIN ZUBAIR SYED[†], C. FARQUHARSON[‡], AND S. MACLACHLAN[§]

Abstract. Geophysical electromagnetic (EM) methods are an important technique for investigating the subsurface of the Earth, particularly when exploring for metallic ore deposits but also when delineating hydrocarbon reserves and in hydrological and geotechnical applications. Geophysical EM methods provide information on subsurface structure from depths of meters to hundreds of kilometers. Quantitative interpretation of the data from such EM methods, whether via trial-and-error forward modeling or inversion, requires the solution of many *forward problems*, simulating EM fields in candidate models of the Earth's subsurface. In this paper, we consider the solution of the linear systems of equations that arise from finite-element discretization of such forward problems, in the setting where the Helmholtz decomposition of the electric field intensity is needed for the inversion process. In particular, a block preconditioning framework is proposed for the equivalent real form of the resulting modeling equations. Particular attention is paid to the interaction between inner and outer Krylov iterations in the resulting preconditioner, and numerical results are presented that explore the balance between time-to-solution and iterations of the outer Krylov method.

Key words. geophysical electromagnetics, preconditioned GMRES, auxilliary-space Maxwell solver, block preconditioning techniques

AMS subject classifications. 86-08, 65F08, 65N55

DOI. 10.1137/19M1241611

1. Introduction. Exploration for metal ores and, to a lesser extent, delineation of hydrocarbon reserves, exploration for and assessment of groundwater resources, and monitoring carbon sequestration all rely on geophysical electromagnetic techniques to image the Earth's subsurface in a region of interest [19, 46, 53, 54, 55]. As is common in exploration geophysics, there are two phases to geophysical electromagnetic methods: data collection and interpretation. In the interpretation phase, an inverse problem is solved, to determine a model of the Earth's subsurface that matches (to some tolerance) the collected data when simulated numerically. While the inverse problem itself involves nontrivial computational effort, a substantial part of the computational cost arises from repeated solution of the related forward problem. In the case of electromagnetics, this requires solution of a discretization of Maxwell's equations with variable coefficients over large regions of the Earth, to see if the simulated data corresponds accurately to that recorded in the original geophysical survey [8, 15, 48].

As is well-recognized, efficient and accurate numerical solution of Maxwell's equations is a difficult task. Here, we consider a finite-element discretization using Nédélec

*Submitted to the journal's Computational Methods in Science and Engineering section January 30, 2019; accepted for publication (in revised form) February 13, 2020; published electronically May 20, 2020.

<https://doi.org/10.1137/19M1241611>

Funding: The work of the third author was supported by the Research and Development Corporation of Newfoundland and Labrador, under Ignite R&D project 5404-1959-101, and by the Hibernia Project Geophysics Support Fund. The work of the third author was partially supported by an NSERC Discovery Grant.

[†]Mathematical Sciences, I.B.A., Karachi, Pakistan (hbinzubair@iba.edu.pk).

[‡]Earth Sciences, Memorial University of Newfoundland, St. John's, NL, A1C 5S7, Canada (cifarquh@mun.ca).

[§]Department of Mathematics and Statistics, Memorial University of Newfoundland, St. John's, Newfoundland, A1C 5S7, Canada (smaclachlan@mun.ca).

elements [35, 44, 47], primarily driven by the need to consider unstructured meshes to accurately resolve realistic models of the Earth's subsurface [4, 24, 28]. Because much geophysical electromagnetic data is measured for sinusoidally varying transmitter currents of prescribed, distinct frequencies, and that which is measured as a time decay following an abrupt shut-off in the transmitter current can be synthesized by a Fourier transform of the frequency domain response, we consider the equations in the frequency domain. While recent years have seen more concerted development of native complex-valued linear solvers [7, 18, 41, 49], these efforts have still not extended into many linear solver packages (including the routines from Hypre [1] used here) and, so, this necessitates the use of the equivalent real form of the discretized PDEs [9, 14, 20, 37, 43]. Further complicating the forward solves in this setting is the desire to resolve not the solution of Maxwell's equations itself but the Helmholtz decomposition of the solution [4, 5, 34].

Taken together, these complicating factors lead to linear systems that require far more sophisticated preconditioners than the block-diagonal and block-triangular preconditioners often considered for block-structured linear systems [7, 14, 29, 45]. Indeed, in [4, 5], simple black-box preconditioners, such as ILU, are used to solve the resulting systems, requiring (tens of) thousands of iterations of restarted GMRES and substantial computational times even for small linear systems. In this paper, our focus is on developing a preconditioning framework suitable for solution of the coupled system of equations resulting from the equivalent real form of Maxwell's equations applied to the Helmholtz decomposition of the electric field. We note two aspects that differ significantly from related work in the literature, such as [29, 43]. First, we do not neglect the permittivity constant, leading to an indefinite shift in some regions of the physical domain. Second, by directly solving for the Helmholtz decomposition of the solution, we must appropriately account for the tight coupling between the scalar and vector potentials in the preconditioner.

The remainder of this paper is organized as follows. In section 2, the continuum model is presented, including the transformation from time to frequency domain and the decomposition of the electric field. The finite-element discretization is presented in section 3. The block preconditioning framework is discussed in section 4, with particular attention paid to the derivation of an approximate Schur complement at the continuum level. Numerical results for several model problems are presented in section 5. Concluding remarks follow in section 6.

2. The continuum (PDE) model. As with any electromagnetic problem, the fundamental model of geophysical electromagnetics is given by Maxwell's equations,

$$(2.1) \quad \nabla \times \mathbf{E}(t) = -\frac{\partial \mathbf{B}(t)}{\partial t} \quad \text{Faraday's law,}$$

$$(2.2) \quad \nabla \times \mathbf{H}(t) = \frac{\partial \mathbf{D}(t)}{\partial t} + \mathbf{J}(t) \quad \text{Ampere's law,}$$

$$(2.3) \quad \nabla \cdot \mathbf{D}(t) = \rho \quad \text{Gauss's law,}$$

$$(2.4) \quad \nabla \cdot \mathbf{B}(t) = 0 \quad \text{Gauss's law (magnetic).}$$

Here, the five unknown functions are $\mathbf{E}(t)$, the electric field intensity (in units of Volts/meter), $\mathbf{D}(t)$, the electric flux density (Coulombs/meter²), $\mathbf{H}(t)$, the magnetic field intensity (Amperes/meter), $\mathbf{B}(t)$, the magnetic flux density (Webers/meter²), and $\mathbf{J}(t)$, the electric current density (Amperes / meter²), while ρ is the electric

charge density (Coulombs/meter³). Taken alone, these yield an undetermined system that is closed by the use of fixed constitutive relations, which we take to be

$$(2.5) \quad \mathbf{D}(t) = \epsilon \mathbf{E}(t),$$

$$(2.6) \quad \mathbf{B}(t) = \mu \mathbf{H}(t), \text{ and}$$

$$(2.7) \quad \mathbf{J}(t) = \mathbf{J}_s(t) + \sigma \mathbf{E}(t).$$

Here, \mathbf{J}_s is the imposed source current, while the physical parameters are ϵ , the electric permittivity (Farads/meter), μ , the magnetic permeability (Henries/meter), and σ , the electrical conductivity (Siemens/meter). In the geophysical electromagnetic context, ϵ and μ are well-represented as constants, with $\mu = 4\pi \times 10^{-7}$ (the permeability of free space) and $\epsilon = 8.854 \times 10^{-12}$ (the permittivity of free space). In contrast, σ varies between materials and, consequently, will be considered to be a piecewise constant function; likewise for the applications considered in this work, ϵ and μ are also constants independent of time and frequency.

We follow a standard approach in reducing the coupled system (2.1) through (2.4), by applying the curl operator to (2.1), exchanging spatial and temporal derivatives on the right-hand side, and then substituting the constitutive relation in (2.6) to give

$$\nabla \times \nabla \times \mathbf{E} = -\mu \frac{\partial}{\partial t} (\nabla \times \mathbf{H}).$$

Substituting (2.2) on the right-hand side yields

$$\nabla \times \nabla \times \mathbf{E} = -\mu \frac{\partial}{\partial t} \left(\frac{\partial \mathbf{D}(t)}{\partial t} + \mathbf{J}(t) \right).$$

Finally, substituting (2.5) and (2.7) for \mathbf{D} and \mathbf{J} , respectively, yields

$$(2.8) \quad \begin{aligned} \nabla \times \nabla \times \mathbf{E} &= -\frac{\partial}{\partial t} \left(\mu \mathbf{J}_s + \mu \sigma \mathbf{E} + \mu \epsilon \frac{\partial \mathbf{E}}{\partial t} \right) \\ &\Rightarrow \nabla \times \nabla \times \mathbf{E} + \mu \sigma \frac{\partial \mathbf{E}}{\partial t} + \mu \epsilon \frac{\partial^2 \mathbf{E}}{\partial t^2} = -\mu \frac{\partial \mathbf{J}_s}{\partial t}. \end{aligned}$$

We take (2.8), the electromagnetic wave equation, as the governing equation in geophysical electromagnetics. In typical geophysical settings, the source current, \mathbf{J}_s , is harmonic in time with angular frequency, ω . With this (and homogeneous boundary conditions), \mathbf{E} is also time harmonic. Writing $\mathbf{J}_s(t) = \hat{\mathbf{J}}_s e^{i\omega t}$ and $\mathbf{E}(t) = \hat{\mathbf{E}} e^{i\omega t}$, the above equation can be written in the frequency domain as

$$\nabla \times \nabla \times \hat{\mathbf{E}} + i\omega \mu \sigma \hat{\mathbf{E}} - \omega^2 \mu \epsilon \hat{\mathbf{E}} = -i\omega \mu \hat{\mathbf{J}}_s.$$

Henceforth, only this form of the equation is used; thus, without compromising clarity, we drop the “hat” notation and rewrite the above as

$$(2.9) \quad \nabla \times \nabla \times \mathbf{E} + i\omega \mu \sigma \mathbf{E} - \omega^2 \mu \epsilon \mathbf{E} = -i\omega \mu \mathbf{J}_s,$$

where \mathbf{E} and \mathbf{J}_s now stand for the time-harmonic components of the electric field intensity and source current density.

While many geophysical techniques make direct use of the total electric field, \mathbf{E} , there have been several recent developments in the literature that make use of a

weighted Helmholtz decomposition, writing the total electric field in terms of a vector and scalar potential, as

$$(2.10) \quad \mathbf{E} = -i\omega \mathbf{A} - \nabla\phi,$$

where \mathbf{A} is divergence-free and ϕ is a scalar field. From a physical viewpoint, the divergence-free and curl-free parts of this decomposition can be associated with so-called inductive and galvanic effects, respectively, which can help us understand the behavior of geophysical electromagnetic methods [27, 56]. At one extreme, in the zero-frequency, constant-current limit (i.e., the DC resistivity method in geophysics), current flows through the subsurface, preferentially channeled through zones of higher conductivity and avoiding zones of lower conductivity. At the other extreme, in a nonconducting background, electric currents are induced to flow in a conductive zone by the time-varying magnetic field produced by the source. Both these effects are present and mutually interacting in the general geophysical electromagnetic scenario. One approach to enable the geophysical analysis would, then, be to solve (2.9) for \mathbf{E} , then to postprocess this vector field, first solving Poisson's equation for the scalar potential, as $-\nabla \cdot \nabla\phi = \nabla \cdot \mathbf{E}$, then computing $\mathbf{A} = \frac{1}{-i\omega}(\mathbf{E} + \nabla\phi)$. Unfortunately, this approach is open to significant loss of accuracy, as it requires first computing the divergence of \mathbf{E} , which naturally lives in $H(\text{curl})$ for a standard finite-element approximation to (2.9), then computing $\nabla\phi$, which naturally yields lower-order accuracy for \mathbf{A} than ϕ , due to the usual difference in order of approximation between $\phi \in H^1$ and its gradient.

Instead, we aim to make this substitution in (2.9) and directly solve for \mathbf{A} and ϕ in their natural spaces. Doing this, we arrive at a single (vector) equation in two unknowns, which is closed by also imposing the Coulomb gauge condition that $\nabla \cdot \mathbf{A} = 0$. While we could aim to solve this as a saddle-point system,

$$\begin{aligned} \nabla \times \nabla \times \mathbf{A} + (i\omega\mu\sigma - \omega^2\mu\varepsilon)\mathbf{A} + (\mu\sigma + i\omega\mu\varepsilon)\nabla\phi &= \mu\mathbf{J}_s, \\ \nabla \cdot \mathbf{A} &= 0, \end{aligned}$$

a more common approach is to add a weighted version of this constraint to the equation of conservation of charge, which is obtained by taking the divergence of (2.9) in the new variables. After slight rescaling, the two resulting governing equations are

$$(2.11) \quad \nabla \times \nabla \times \mathbf{A} + (i\omega\mu\sigma - \omega^2\mu\varepsilon)\mathbf{A} + (\mu\sigma + i\omega\mu\varepsilon)\nabla\phi = \mu\mathbf{J}_s,$$

$$(2.12) \quad -i\omega\nabla \cdot (\sigma\mathbf{A}) + \omega^2\nabla \cdot (\varepsilon\mathbf{A}) - \nabla \cdot (\sigma\nabla\phi) - i\omega\nabla \cdot (\varepsilon\nabla\phi) + \alpha(\nabla \cdot \mathbf{A}) = -\nabla \cdot \mathbf{J}_s,$$

which we refer to as the implicitly gauged model. Here, the dimensionless parameter α may be any real or complex gauging constant, used to control the relative weight between the Coulomb gauge condition and the equation of conservation of charge. In this gauged formulation of the continuum equation, the value of α is immaterial as long as it is not identically zero. In the discrete setup, however, the choice of α can make a practical difference, particularly in the form of the approximate Schur complement considered below in section 4.3. In the experiments that follow, we set this gauging constant as $\alpha = \alpha_r + \alpha_i i$, with $\alpha_r = 0.0$, and $\alpha_i = 0.0625$. As (4.6) will show, the choice of purely imaginary α leads to a preferential structure to the Schur complement. Numerical experiments show that the preconditioner behaves similarly for any (nonzero) value of α_i , when α_r is chosen to be zero.

3. Finite-element discretization. Due to prevailing software limitations (including in FEniCS 2017.2.0, as used in this work [3, 38]), we follow the path of first writing (2.11) and (2.12) in the continuum equivalent real form, then discretizing using the finite-element method with real-valued discrete degrees of freedom. We note, however, that the order of these operations is immaterial and that the same linear system would arise if the PDEs are first discretized using complex-valued finite-element coefficients, and then the equivalent real form of the discretized system is assembled. To rewrite (2.11) and (2.12) in the continuum equivalent real form, we replace \mathbf{A} and ϕ in these equations by $\mathbf{A} = \mathbf{A}_r + i\mathbf{A}_i$ and $\phi = \phi_r + i\phi_i$, where \mathbf{A}_r and \mathbf{A}_i are real-valued vector fields and ϕ_r and ϕ_i are real-valued functions. With these substitutions, (2.11) becomes

(3.1)

$$\begin{aligned} \nabla \times \nabla \times \mathbf{A}_r + i\nabla \times \nabla \times \mathbf{A}_i - \omega\mu\sigma\mathbf{A}_i - \omega^2\mu\varepsilon\mathbf{A}_r + i\omega\mu\sigma\mathbf{A}_r - i\omega^2\mu\varepsilon\mathbf{A}_i \\ + \mu\sigma\nabla\phi_r - \omega\mu\varepsilon\nabla\phi_i + i\omega\mu\varepsilon\nabla\phi_r + i\mu\sigma\nabla\phi_i = \mu\mathbf{J}_s. \end{aligned}$$

Similarly, (2.12) takes the form

(3.2)

$$\begin{aligned} \omega^2\nabla \cdot (\varepsilon\mathbf{A}_r) + (\alpha_r + i\alpha_i)\nabla \cdot (\mathbf{A}_r) - i\omega\nabla \cdot (\sigma\mathbf{A}_r) \\ + \omega\nabla \cdot (\sigma\mathbf{A}_i) + i\omega^2\nabla \cdot (\varepsilon\mathbf{A}_i) + i(\alpha_r + i\alpha_i)\nabla \cdot \mathbf{A}_i \\ - \nabla \cdot \sigma(\nabla\phi_r) - i\omega\nabla \cdot (\varepsilon\nabla\phi_r) + \omega\nabla \cdot \varepsilon(\nabla\phi_i) - i\nabla \cdot \sigma(\nabla\phi_i) = -\nabla \cdot \mathbf{J}_s. \end{aligned}$$

Assuming a real-valued source field, \mathbf{J}_s , we separate the real and imaginary parts of (3.1) and (3.2) into four coupled real-valued PDEs,

$$(3.3) \quad \nabla \times \nabla \times \mathbf{A}_r - \omega^2\mu\varepsilon\mathbf{A}_r - \omega\mu\sigma\mathbf{A}_i + \mu\sigma\nabla\phi_r - \omega\mu\varepsilon\nabla\phi_i = \mu\mathbf{J}_s,$$

$$(3.4) \quad \omega\mu\sigma\mathbf{A}_r + \nabla \times \nabla \times \mathbf{A}_i - \omega^2\mu\varepsilon\mathbf{A}_i + \omega\mu\varepsilon\nabla\phi_r + \mu\sigma\nabla\phi_i = 0,$$

$$(3.5) \quad \omega^2\nabla \cdot (\varepsilon\mathbf{A}_r) + \alpha_r\nabla \cdot \mathbf{A}_r + \omega\nabla \cdot (\sigma\mathbf{A}_i) - \alpha_i\nabla \cdot \mathbf{A}_i$$

$$- \nabla \cdot \sigma(\nabla\phi_r) + \omega\nabla \cdot \varepsilon(\nabla\phi_i) = -\nabla \cdot \mathbf{J}_s,$$

$$(3.6) \quad - \omega\nabla \cdot (\sigma\mathbf{A}_r) + \alpha_i\nabla \cdot \mathbf{A}_r + \omega^2\nabla \cdot (\varepsilon\mathbf{A}_i) + \alpha_r\nabla \cdot \mathbf{A}_i$$

$$- \omega\nabla \cdot (\varepsilon\nabla\phi_r) - \nabla \cdot \sigma(\nabla\phi_i) = 0.$$

The discretization of these equations is done using a standard Galerkin finite-element method (see, for example, [16, 17]) applied to the coupled system in (3.3) through (3.6). Since the dominant differential operators in (3.3) and (3.4) are curl-curl operators, we consider $\mathbf{A}_r, \mathbf{A}_i \in H(\text{curl})$ and discretize using lowest-order Nédélec edge elements, while the scalar fields ϕ_r, ϕ_i are discretized using piecewise linear Lagrange elements. We use vector test functions $\hat{\mathbf{A}}_r$ and $\hat{\mathbf{A}}_i$ for (3.3) and (3.4), respectively, and scalar test functions $\hat{\phi}_r$ and $\hat{\phi}_i$ for (3.5) and (3.6), respectively. The standard integration by parts (Stokes theorem) identities are used here,

$$(a) \int_{\Omega} \mathbf{w} \cdot \nabla \times \mathbf{u} \, dV = \int_{\Omega} \mathbf{u} \cdot \nabla \times \mathbf{w} \, dV + \int_{\partial\Omega} \mathbf{u} \cdot (\mathbf{w} \times \hat{\mathbf{n}}) \, dA,$$

$$(b) \int_{\Omega} v \nabla \cdot \mathbf{w} \, dV = - \int_{\Omega} \nabla v \cdot \mathbf{w} \, dV + \int_{\partial\Omega} v (\mathbf{w} \cdot \hat{\mathbf{n}}) \, dA,$$

where \mathbf{u} and \mathbf{w} are real vector-valued functions and v is a real-valued function, integrated over the domain Ω enclosed by the boundary $\partial\Omega$ with unit outward normal vector $\hat{\mathbf{n}}$. For the examples considered here, we assume homogeneous Dirichlet boundary conditions on all components of the solution and, consequently, the boundary integrals vanish. We note, however, that this could be easily adapted for other

boundary conditions that are typical in geophysical electromagnetics, such as those needed to model plane wave sources.

The corresponding weak forms to (3.3) through (3.6) are then given by

(3.7)

$$c(\mathbf{A}_r, \hat{\mathbf{A}}_r) - \omega^2 \mu m_\varepsilon(\mathbf{A}_r, \hat{\mathbf{A}}_r) - \omega \mu m_\sigma(\mathbf{A}_i, \hat{\mathbf{A}}_r) + \mu p_\sigma(\phi_r, \hat{\mathbf{A}}_r) - \omega \mu p_\varepsilon(\phi_i, \hat{\mathbf{A}}_r) = \mu \int_{\Omega} \mathbf{J}_s \cdot \hat{\mathbf{A}}_r \, dV,$$

(3.8)

$$\omega \mu m_\sigma(\mathbf{A}_r, \hat{\mathbf{A}}_i) + c(\mathbf{A}_i, \hat{\mathbf{A}}_i) - \omega^2 \mu m_\varepsilon(\mathbf{A}_i, \hat{\mathbf{A}}_i) + \omega \mu p_\varepsilon(\phi_r, \hat{\mathbf{A}}_i) + \mu p_\sigma(\phi_i, \hat{\mathbf{A}}_i) = 0,$$

(3.9)

$$-\omega^2 p_\varepsilon(\hat{\phi}_r, \mathbf{A}_r) - \alpha_r p(\hat{\phi}_r, \mathbf{A}_r) - \omega p_\sigma(\hat{\phi}_r, \mathbf{A}_i) + \alpha_i p(\hat{\phi}_r, \mathbf{A}_i) + r_\sigma(\phi_r, \hat{\phi}_r) - \omega r_\varepsilon(\phi_i, \hat{\phi}_r) = \int_{\Omega} \nabla \hat{\phi}_r \cdot \mathbf{J}_s \, dV,$$

(3.10)

$$\omega p_\sigma(\hat{\phi}_i, \mathbf{A}_r) - \alpha_i p(\hat{\phi}_i, \mathbf{A}_r) - \omega^2 p_\varepsilon(\hat{\phi}_i, \mathbf{A}_i) - \alpha_r p(\hat{\phi}_i, \mathbf{A}_i) + \omega r_\varepsilon(\phi_r, \hat{\phi}_i) + r_\sigma(\phi_i, \hat{\phi}_i) = 0,$$

where

$$c(\mathbf{A}, \hat{\mathbf{A}}) = \int_{\Omega} \nabla \times \mathbf{A} \cdot \nabla \times \hat{\mathbf{A}} \, dV,$$

$$m_\varepsilon(\mathbf{A}, \hat{\mathbf{A}}) = \int_{\Omega} \varepsilon \mathbf{A} \cdot \hat{\mathbf{A}} \, dV, \quad m_\sigma(\mathbf{A}, \hat{\mathbf{A}}) = \int_{\Omega} \sigma \mathbf{A} \cdot \hat{\mathbf{A}} \, dV,$$

$$p_\sigma(\phi, \hat{\mathbf{A}}) = \int_{\Omega} \sigma \nabla \phi \cdot \hat{\mathbf{A}} \, dV = - \int_{\Omega} \phi \nabla \cdot (\sigma \hat{\mathbf{A}}) \, dV,$$

$$p_\varepsilon(\phi, \hat{\mathbf{A}}) = \int_{\Omega} \varepsilon \nabla \phi \cdot \hat{\mathbf{A}} \, dV = - \int_{\Omega} \phi \nabla \cdot (\varepsilon \hat{\mathbf{A}}) \, dV,$$

$$p(\hat{\phi}, \mathbf{A}) = - \int_{\Omega} \hat{\phi} \nabla \cdot \mathbf{A} \, dV,$$

$$r_\sigma(\phi, \hat{\phi}) = \int_{\Omega} \sigma \nabla \phi \cdot \nabla \hat{\phi} \, dV, \quad r_\varepsilon(\phi, \hat{\phi}) = \int_{\Omega} \varepsilon \nabla \phi \cdot \nabla \hat{\phi} \, dV.$$

In what follows, we assume that a tetrahedral mesh of the three-dimensional volume, Ω , is given and that jumps in the piecewise constant coefficient, σ , are perfectly aligned with faces of elements in the mesh. This will be the case in the examples considered below, where the mesh is generated to ensure this property. On such a mesh, standard finite-element discretization and assembly processes are used to translate the weak forms in (3.7) through (3.10) into the discrete system that needs to be solved. The resulting discrete equations, $\mathcal{A}\vec{x} = \vec{b}$, are naturally written in 4×4 block form. In what follows, we reverse the sign on (3.8) so that the upper left 2×2 block structure is symmetric. With this, the discrete operator is written as

(3.11)

$$\left[\begin{array}{cc|cc} C - \omega^2 \mu M_\varepsilon & -\omega \mu M_\sigma & \mu P_\sigma & -\omega \mu P_\varepsilon \\ -\omega \mu M_\sigma & -C + \omega^2 \mu M_\varepsilon & -\omega \mu P_\varepsilon & -\mu P_\sigma \\ \hline -\omega^2 P_\varepsilon^T - \alpha_r P^T & -\omega P_\sigma^T + \alpha_i P^T & R_\sigma & -\omega R_\varepsilon \\ \omega P_\sigma^T - \alpha_i P^T & -\omega^2 P_\varepsilon^T - \alpha_r P^T & \omega R_\varepsilon & R_\sigma \end{array} \right] \begin{bmatrix} \vec{A}_r \\ \vec{A}_i \\ \vec{\phi}_r \\ \vec{\phi}_i \end{bmatrix} = \begin{bmatrix} \vec{b}_1 \\ \vec{0} \\ \vec{b}_3 \\ \vec{0} \end{bmatrix},$$

where C is the stiffness matrix associated with $c(\cdot, \cdot)$, M_ε and M_σ are the mass matrices associated with $m_\varepsilon(\cdot, \cdot)$ and $m_\sigma(\cdot, \cdot)$ respectively, P_ε , P_σ , and P are the matrices associated with the weak forms $p_\varepsilon(\cdot, \cdot)$, $p_\sigma(\cdot, \cdot)$, and $p(\cdot, \cdot)$, respectively, and R_ε and R_σ are the stiffness matrices associated with $r_\varepsilon(\cdot, \cdot)$ and $r_\sigma(\cdot, \cdot)$, respectively. We write \vec{A}_r , \vec{A}_i , $\vec{\phi}_r$, and $\vec{\phi}_i$ as the vectors of coefficients of the finite-element approximations of the respective functions. From the right-hand sides of (3.7) and (3.9), we write \vec{b}_1 as the discretized form of $\mu \int_\Omega J_s \cdot \hat{\mathbf{A}}_r dV$ and \vec{b}_3 as the discretized form of $\int_\Omega \nabla \hat{\phi}_r \cdot \mathbf{J}_s dV$. For the other two components of \vec{b} , we write $\vec{0}$ to represent all-zero vectors of appropriate dimension.

4. Preconditioning the discretized system. Solution of the linear system given in (3.11) is nontrivial. Achieving accuracy in simulating the underlying geophysical electromagnetic surveys may require very large meshes that make direct methods impractical, even in parallel, due to memory requirements. Experiments in [5] show that, even for small meshes, preconditioned iterative methods can outperform direct solvers in terms of total time-to-solution. Achieving an efficient iterative solution is, however, also not straightforward, and results in [4, 5] show that standard ILU-preconditioned GMRES struggles to solve the resulting linear systems. There are several contributing factors to this. First of all, the Coulomb gauge condition, used to ensure uniqueness of the Helmholtz decomposition of the solution, is an inherently nonsymmetric term in the system. Second, the first two diagonal blocks are indefinite, due to the large null-space of the curl-curl stiffness matrix, C , and the indefinite shift by $\omega^2 \mu M_\varepsilon$. We note that while ε is uniformly small, ω may be quite large (as it is in some of the numerical results to follow) and, consequently, this term cannot be neglected. Finally, preliminary numerical experiments (not reported here) show that the off-diagonal coupling in the system is significant enough that both block-diagonal and block-triangular preconditioners fail to lead to robust iterative methods.

The central contribution of this paper is to develop a robust block preconditioning strategy for (3.11). Due to the failure of block-diagonal and block-triangular preconditioners, we use a block-factorization preconditioner, described in section 4.1, based on viewing the system as a 2×2 block matrix with 2×2 blocks. Preconditioning for the upper left 2×2 block, associated with the \mathbf{A}_r and \mathbf{A}_i degrees of freedom, is discussed in section 4.2. Derivation of an operator-based Schur complement onto the ϕ_r and ϕ_i degrees of freedom and a preconditioning strategy for the resulting discrete system are presented in section 4.3. Finally, the nesting of the inner-outer preconditioning strategy is described in detail in section 4.4.

4.1. The approximate LU preconditioner. Preliminary experiments (not included here) showed that, even with exact subsolves of the constituent blocks, classical block-diagonal or block-triangular preconditioners are ineffective for this system. This is quite likely due to the practical need for sparse approximation of the Schur complement (discussed below) as well as the nonsymmetry and indefiniteness of the equivalent real form considered here. We write the linear system in (3.11) as $\mathcal{A}\vec{x} = \vec{b}$, in block 2×2 form as

$$(4.1) \quad \mathcal{A} = \begin{bmatrix} \mathcal{A}_{11} & \mathcal{A}_{12} \\ \mathcal{A}_{21} & \mathcal{A}_{22} \end{bmatrix}, \quad \mathcal{P}_L = \begin{bmatrix} \mathcal{A}_{11} & \mathbf{0} \\ \mathcal{A}_{21} & \mathcal{S} \end{bmatrix}, \quad \mathcal{P}_U = \begin{bmatrix} I & \mathcal{A}_{11}^{-1} \mathcal{A}_{12} \\ \mathbf{0} & I \end{bmatrix},$$

with its block LU factorization given as $\mathcal{A} = \mathcal{P}_L \mathcal{P}_U$, where I represents appropriately sized identity matrices and $\mathcal{S} = \mathcal{A}_{22} - \mathcal{A}_{21} \mathcal{A}_{11}^{-1} \mathcal{A}_{12}$. Here,

$$\begin{aligned}\mathcal{A}_{11} &= \begin{bmatrix} C - \omega^2 \mu M_\varepsilon & -\omega \mu M_\sigma \\ -\omega \mu M_\sigma & -C + \omega^2 \mu M_\varepsilon \end{bmatrix}; & \mathcal{A}_{12} &= \begin{bmatrix} \mu P_\sigma & -\omega \mu P_\varepsilon \\ -\omega \mu P_\varepsilon & -\mu P_\sigma \end{bmatrix}, \\ \mathcal{A}_{21} &= \begin{bmatrix} -\omega^2 P_\varepsilon^T - \alpha_r P^T & -\omega P_\sigma^T + \alpha_i P^T \\ \omega P_\sigma^T - \alpha_i P^T & -\omega^2 P_\varepsilon^T - \alpha_r P^T \end{bmatrix}; & \mathcal{A}_{22} &= \begin{bmatrix} R_\sigma & -\omega R_\varepsilon \\ \omega R_\varepsilon & R_\sigma \end{bmatrix}.\end{aligned}$$

To solve the matrix equation $\mathcal{A}\vec{x} = \vec{b}$, we will use flexible GMRES (FGMRES) *right preconditioned* by $(\hat{\mathcal{P}}_L \hat{\mathcal{P}}_U)^{-1}$, where the terms in the preconditioner are defined by suitable approximations to the LU factors,

$$\hat{\mathcal{P}}_L = \begin{bmatrix} \hat{\mathcal{A}}_{11} & \mathbf{0} \\ \mathcal{A}_{21} & \hat{\mathcal{S}} \end{bmatrix}, \quad \hat{\mathcal{P}}_U = \begin{bmatrix} I & \hat{\mathcal{A}}_{11}^{-1} \mathcal{A}_{12} \\ \mathbf{0} & I \end{bmatrix}.$$

Sections 4.2 and 4.3 describe the approximations made for $\hat{\mathcal{A}}_{11}$ and $\hat{\mathcal{S}}$, respectively. As with any Krylov method, we must be able to apply this preconditioner to an arbitrary block vector $\vec{v} = [\vec{v}_1, \vec{v}_2]^T$, and we can compute

$$\begin{aligned}(4.2) \quad (\hat{\mathcal{P}}_L \hat{\mathcal{P}}_U)^{-1} \begin{bmatrix} \vec{v}_1 \\ \vec{v}_2 \end{bmatrix} &= \begin{bmatrix} I & \hat{\mathcal{A}}_{11}^{-1} \mathcal{A}_{12} \\ \mathbf{0} & I \end{bmatrix}^{-1} \begin{bmatrix} \hat{\mathcal{A}}_{11} & \mathbf{0} \\ \mathcal{A}_{21} & \hat{\mathcal{S}} \end{bmatrix}^{-1} \begin{bmatrix} \vec{v}_1 \\ \vec{v}_2 \end{bmatrix} \\ &= \begin{bmatrix} \hat{\mathcal{A}}_{11}^{-1} [\vec{v}_1 - \mathcal{A}_{12} \hat{\mathcal{S}}^{-1} \{-\mathcal{A}_{21}(\hat{\mathcal{A}}_{11}^{-1} \vec{v}_1) + \vec{v}_2\}] \\ \hat{\mathcal{S}}^{-1} \{-\mathcal{A}_{21}(\hat{\mathcal{A}}_{11}^{-1} \vec{v}_1) + \vec{v}_2\} \end{bmatrix}.\end{aligned}$$

Thus, the application of the preconditioner to compute $\vec{z} = (\hat{\mathcal{P}}_L \hat{\mathcal{P}}_U)^{-1} \vec{v}$ can be done in three steps, corresponding to two solves with $\hat{\mathcal{A}}_{11}$ and one with $\hat{\mathcal{S}}$:

1. Solve $\hat{\mathcal{A}}_{11} \vec{y}_1 = \vec{v}_1$.
2. Solve $\hat{\mathcal{S}} \vec{z}_2 = \vec{v}_2 - \mathcal{A}_{21} \vec{y}_1$.
3. Solve $\hat{\mathcal{A}}_{11} \vec{z}_1 = \vec{v}_1 - \mathcal{A}_{12} \vec{z}_2$.

Note that, equivalently, the third step could solve for $\hat{\mathcal{A}}_{11}^{-1} \mathcal{A}_{12} \vec{z}_2$ and subtract this from \vec{y}_1 , which is how this step is implemented in practice.

4.2. Preconditioning the curl-curl block. Efficient multigrid solvers for the Nédélec finite-element discretization of a scalar curl-curl operator were first proposed in [6, 30] and have been adapted and extended in many contexts since then [29, 31, 33, 36]. Here, we follow the auxiliary-space preconditioning (or Hiptmair–Xu) formulation as discussed in [31] and implemented as the auxiliary-space Maxwell solver (AMS) algorithm in Hypre [1, 36].

For a scalar curl-curl operator, such as the eddy-current form of Maxwell's equations,

$$c(\mathbf{A}, \hat{\mathbf{A}}) + m_\sigma(\mathbf{A}, \hat{\mathbf{A}}) = \int_{\Omega} \mathbf{J}_s \cdot \hat{\mathbf{A}} dV,$$

optimal convergence of AMS-preconditioned conjugate gradients (when $\sigma \geq 0$, for example, so the discretized operator is symmetric and positive semidefinite) is well

understood; see [36]. The three stages of the auxiliary-space approach for such an operator are

- relaxation on the Nédélec discretization matrix as given, $C + M_\sigma$,
- multigrid applied to the vector (diffusion-like) operator arising from the Galerkin projection of $C + M_\sigma$ into the standard (vector) finite-element space for $(H^1(\Omega))^3$ of equal order to the Nédélec basis functions, using the canonical finite-element interpolation operator, and
- multigrid applied to the scalar diffusion operator arising from discretizing the weak form $r_\sigma(\phi, \hat{\phi})$, for $\phi, \hat{\phi}$ in the standard (scalar) finite-element space for $H^1(\Omega)$ of equal order to the Nédélec basis functions.

Of course, the details of the relaxation and multigrid algorithms chosen make a great difference in the efficiency and robustness of the resulting auxiliary-space preconditioner. Here, we use a symmetric, multiplicative sweep, where we first relax on the Nédélec discretization, then apply multigrid to the vector diffusion operator, then to the scalar diffusion operator, then again to the vector diffusion operator, and, finally, relax again on the Nédélec discretization. For the Nédélec relaxation, we use three sweeps of ℓ_1 -scaled block symmetric Gauss–Seidel (the default in Hypre; see, for instance, [10]). For the vector diffusion operator, since the problem has constant diffusion coefficient, we solve it sequentially by applying scalar multigrid to each of the three components of the solution, ordered as the x -component, then the y -component, then the z -component on the first pass, and in opposite (symmetric) order on the second pass. For all scalar multigrid cycles, we use ℓ_1 -scaled Jacobi as the relaxation scheme, with classical (Ruge–Stüben) coarsening with strength threshold 0.3 and a multipass interpolation operator restricted to five nonzero entries per row. These options were selected via numerical experiments for best overall performance.

To extend the AMS solver from the real-valued eddy-current problem above, we follow [29] and define an idealized block-diagonal preconditioner for \mathcal{A}_{11} of the form

$$\tilde{\mathcal{A}}_{11} = \begin{bmatrix} C + \omega\mu M_\sigma - \omega^2\mu M_\varepsilon & 0 \\ 0 & C + \omega\mu M_\sigma - \omega^2\mu M_\varepsilon \end{bmatrix}.$$

In practice, either a stationary or a Krylov-accelerated AMS cycle is employed to approximately invert each of the diagonal blocks of $\tilde{\mathcal{A}}_{11}$, and we denote the resulting approximate inverse operator as $\hat{\mathcal{A}}_{11}^{-1}$. A key difference between the real-valued eddy-current problem above and the $\varepsilon = 0$ case considered in [29] is that the matrix $C + \omega\mu M_\sigma - \omega^2\mu M_\varepsilon$ may not be positive-definite, due to negative shift by M_ε . For typical geophysical problems, σ is taken to be quite small (10^{-8} or smaller) in the part of the domain corresponding to air, while $\varepsilon = 8.854 \times 10^{-12}$ everywhere. Clearly, if $\sigma = 10^{-8}$ and $\omega > 1000$ (corresponding to a time-harmonic source with frequency greater than about 200 Hz), then the system is expected to be somewhat indefinite, due to the large singularity of the curl-curl discretization matrix, C . Typical geophysical experiments do run at frequencies in this range and, while there is no theoretical guarantee for the convergence of AMS in the indefinite case, numerical experiments in section 5 illustrate the effects of such indefiniteness and suggest some ways to mitigate them. While some options exist for preconditioners that may outperform AMS on the indefinite system [26, 32], to our knowledge, design of effective solvers for the indefinite case remains an open research question.

4.3. The approximate Schur complement. As with any block-based preconditioner, an important consideration is how to construct an approximation to the

Schur complement in blocked form. Here, we again consider the block 2×2 form of the system as given in (4.1); in that notation, we seek to define $\hat{\mathcal{S}}$ as a suitable approximation to $\mathcal{S} = \mathcal{A}_{22} - \mathcal{A}_{21}\mathcal{A}_{11}^{-1}\mathcal{A}_{12}$. It is well-established in the preconditioning literature that simple approximations of the Schur complement (for example, by approximating \mathcal{A}_{11} by its diagonal) typically lead to poor performance (see, for example, [22, section 8.3.5]). Thus, we instead follow the well-established route of considering the formation of the Schur complement at the continuum level, then discretize this to form the approximate Schur complement [40, 42].

Here, we take advantage of the simpler form of the equations in their original complex arithmetic, writing the operator in block form as

$$(4.3) \quad \begin{bmatrix} \nabla \times \nabla \times + (-\omega^2 \mu \varepsilon + i\omega \mu \sigma) \mathcal{I} & (\mu \sigma + i\omega \mu \varepsilon) \nabla \\ \nabla \cdot ((\omega^2 \varepsilon + \alpha_r) + i(\alpha_i - \omega \sigma)) & \nabla \cdot (-\sigma - i\omega \varepsilon) \nabla \end{bmatrix},$$

where \mathcal{I} represents the continuum identity operator. At the continuum level, the action of the Schur complement on a scalar function, ϕ , is computed by finding a vector field, A , such that

$$(4.4) \quad \nabla \times \nabla \times A + (-\omega^2 \mu \varepsilon + i\omega \mu \sigma) A + (\mu \sigma + i\omega \mu \varepsilon) \nabla \phi = 0,$$

and then computing

$$(4.5) \quad \nabla \cdot (-\sigma - i\omega \varepsilon) \nabla \phi + \nabla \cdot ((\omega^2 \varepsilon + \alpha_r) + i(\alpha_i - \omega \sigma)) A.$$

To satisfy (4.4), we note that the null-space of the curl operator is the gradient and, so, taking $A = c \nabla \phi$ for any constant, c , results in the simple identity

$$[c(-\omega^2 \mu \varepsilon + i\omega \mu \sigma) \nabla + (\mu \sigma + i\omega \mu \varepsilon) \nabla] \phi = 0,$$

which is satisfied by taking $c = i/\omega$. Then, substituting $A = (i/\omega) \nabla \phi$ into (4.5), we have the continuum Schur complement take the form

$$\begin{aligned} & \nabla \cdot (-\sigma - i\omega \varepsilon) \nabla \phi + \nabla \cdot ((\omega^2 \varepsilon + \alpha_r) + i(\alpha_i - \omega \sigma)) \left(\frac{i}{\omega} \nabla \phi \right) \\ &= \nabla \cdot \left[-\frac{\alpha_i}{\omega} + \frac{\alpha_r}{\omega} i \right] \nabla \phi. \end{aligned}$$

This, conveniently, leads to an operator that has a sparse discretization and is independent of the various physical parameters in the PDE system (aside from the angular frequency, ω).

In practice, this continuum Schur complement is approximated in two ways. First, it is discretized in the piecewise linear finite-element space used for ϕ . Second, we approximate its inverse (as needed in (4.2)) by using algebraic multigrid to define $\hat{\mathcal{S}}^{-1}$. When written in equivalent real form, the discretization of the continuum Schur complement is given by

$$(4.6) \quad \tilde{\mathcal{S}} = \frac{1}{\omega} \begin{bmatrix} -R_{\alpha_i} & -R_{\alpha_r} \\ R_{\alpha_r} & -R_{\alpha_i} \end{bmatrix},$$

where R_α is the discretization matrix associated with the weak form $r_\alpha(\phi, \hat{\phi}) = \langle \alpha \nabla \phi, \nabla \hat{\phi} \rangle$. While efficient complex-valued AMG algorithms exist in the literature

[41], since we already are considering the equivalent real form for the overall coupled system, we simply apply AMG directly to the equivalent real form for convenience. As our typical choice is $\alpha_r = 0$, this distinction is even less important, as the off-diagonal coupling disappears. Here, we employ symmetric Gauss–Seidel as the relaxation scheme for W(2,2) cycles, with CLJP coarsening with strength-of-connection parameter 0.8 and “extended+ i ” interpolation. These options were chosen as they yielded the most robust performance in numerical experiments; we note that they are somewhat nonstandard but that this is to be expected due to the extreme amounts of heterogeneity in the computational mesh, even though the discrete operator is a constant-coefficient diffusion equation.

4.4. Iterative framework. We use these components as a right preconditioner for FGMRES [50]. As discussed in section 4.2, we base $\hat{\mathcal{A}}_{11}$ on the idealized block-diagonal preconditioner $\tilde{\mathcal{A}}_{11}$ for the Nédélec degrees of freedom. While this can be done directly within the block-factorization preconditioning framework given in (4.2), it is also possible to nest an inner iteration of FGMRES to solve this subblock. In the numerical results that follow, we consider both possibilities. When a single cycle of AMS on each diagonal block is used directly to approximate $\hat{\mathcal{A}}_{11}^{-1}$, we refer to the overall preconditioning strategy as “Preconditioning-1.” In contrast, “Preconditioning-2” denotes using Krylov acceleration of this AMS cycle within the block-diagonal approximation, $\hat{\mathcal{A}}_{11}$ as a preconditioner for \mathcal{A}_{11} . In the latter case, we use a very “loose” tolerance to control the inner iterations on the equivalent real form of the curl-curl system, asking for a relative reduction in the residual norm of only 10^{-1} or 10^{-2} , following [29]. While the same strategy is possible for the approximate Schur complement inversion, we find that inner Krylov acceleration here is not necessary.

The software setup required to execute these experiments makes use of several tools. Discretization was accomplished using FEniCS, a well-established automated tool for finite-element discretization on tetrahedral meshes in three dimensions [3, 38, 39]. While this might have been interfaced directly with the linear algebra packages below, the python interface was used for convenience, and matrices and vectors written to file in standard formats using the PETSc interface [11]. A wrapper to MFEM [2] was written, to make use of the block-structured linear algebra capability of this library, along with its natural interface to Hypre [1]. The underlying FGMRES iteration from MFEM was used, with AMS and AMG algorithms directly used from Hypre. The block-structured preconditioning algorithms from MFEM were extended to allow full block LU preconditioners.

We summarize the details of the implementation of this solver in Algorithm 4.1, following the notation given in the previous subsections. The settings of the inner AMS and AMG preconditioners are not included directly in the algorithm to save space but have been given in detail in sections 4.2 and 4.3, respectively. The application of the final preconditioner is implemented as described in the three steps following (4.2).

5. Numerical experiments. In this section, we demonstrate the performance of the preconditioning strategy developed in this paper. We test the solver performance with two sets of numerical experiments. The first set of experiments—presented in section 5.1—concern solving the coupled model as in (3.11) with a fabricated solution, on uniform meshes with different mesh sizes, and varying frequencies. We show that the solver works stably in the case when the operator $C + \omega\mu M_\sigma - \omega^2\mu M_\epsilon$ is in the definite or semidefinite regime (noting that, for fixed μ and ϵ , conditions for definiteness are easily expressed as bounds on the frequency, ω), whereas its perfor-

Algorithm 4.1 The APHISOLVER

Input : $\mathcal{A}_{11}, \mathcal{A}_{12}, \mathcal{A}_{21}, \mathcal{A}_{22}, \tilde{\mathcal{A}}_{11}, \tilde{\mathcal{S}}, \vec{x}, \vec{b}$

Output: \vec{x} , CPUtime

Initialize and set up matrices and operators:

set up: $\hat{\mathcal{B}}_1^{-1}$ with:

- $(\tilde{\mathcal{A}}_{11})_{11}$ as operator
- AMS as method (1 cycle)

set up: $\hat{\mathcal{B}}_2^{-1}$ with:

- $(\tilde{\mathcal{A}}_{11})_{11}$ as operator
- FGMRES as method ($TOL = 10^{-1}$, or 10^{-2})
- $\hat{\mathcal{B}}_1^{-1}$ as preconditioner

set up: $\hat{\mathcal{S}}^{-1}$ with:

- $\tilde{\mathcal{S}}$ as operator
- AMG as method ($TOL = 10^{-10}$)

switch P_TYPE:

case 1: (Preconditioning-1)

$$\text{initialize: } \hat{\mathcal{A}}_{11} = \begin{bmatrix} \hat{\mathcal{B}}_1 & 0 \\ 0 & \hat{\mathcal{B}}_1 \end{bmatrix} ;$$

case 2: (Preconditioning-2)

$$\text{initialize: } \hat{\mathcal{A}}_{11} = \begin{bmatrix} \hat{\mathcal{B}}_2 & 0 \\ 0 & \hat{\mathcal{B}}_2 \end{bmatrix} ;$$

$$\text{initialize: } \hat{\mathcal{P}}_U = \begin{bmatrix} I & \hat{\mathcal{A}}_{11}^{-1} \mathcal{A}_{12} \\ 0 & I \end{bmatrix} ;$$

$$\text{initialize: } \hat{\mathcal{P}}_L = \begin{bmatrix} \hat{\mathcal{A}}_{11} & 0 \\ \mathcal{A}_{21} & \hat{\mathcal{S}} \end{bmatrix} ;$$

set up: APHISOLVER with:

- FGMRES as method ($TOL = 10^{-10}$)
- \mathcal{A} as operator
- $\hat{\mathcal{P}}_L^{-1} \hat{\mathcal{P}}_U^{-1}$ as preconditioner
- \vec{b} as the right-hand side
- \vec{x} as the (starting) solution

Start:

Run APHISOLVER until convergence.

Return \vec{x} , CPUtime.

End

mance degrades significantly when this operator becomes indefinite, as anticipated. The second set of experiments—in sections 5.2 and 5.3—concern the three real-world model problems, for which this framework was developed. These problems differ in their algebraic characteristics, and we test the solver with variations in its constituent

components and parameters. The solver behavior on all cases of the model problems that we tested was stable, as well as computationally viable in terms of computational cost compared to the earlier solution method used in [5].

5.1. Uniform mesh refinement study. We first present numerical experiments based on solving the coupled discrete model in the formulation given by (3.11) for nonphysical solutions for the solenoidal function \mathbf{A} and scalar function ϕ ,

$$(5.1) \quad \mathbf{A} = [\cos \pi \tilde{x} \sin \pi \tilde{y} \sin \pi \tilde{z}, -2 \sin \pi \tilde{x} \cos \pi \tilde{y} \sin \pi \tilde{z}, \sin \pi \tilde{x} \sin \pi \tilde{y} \cos \pi \tilde{z}]^T,$$

$$(5.2) \quad \phi = -\sin \pi \tilde{x} \sin \pi \tilde{y} \sin \pi \tilde{z},$$

on uniform meshes. To ensure these tests remain relevant to the geophysical scenarios considered later on, we consider this test problem on an L^3 domain where $L = 100\text{ m}$ and, then, make the problem dimensionless by introducing a change of variables, $x = \tilde{x}/L$, $y = \tilde{y}/L$, $z = \tilde{z}/L$. Rescaling (3.3) through (3.6) appropriately results in terms without derivatives being scaled by a factor of L^2 and first-order derivative terms being scaled by a factor of L , while second-order derivative terms remain unscaled. We apply the operators on the left sides of (3.3) through (3.6) to \mathbf{A} and ϕ (as prescribed in (5.1)), in order to obtain $\mathbf{J}_s(\tilde{x}, \tilde{y}, \tilde{z})$. The real and imaginary parts of $\mathbf{J}_s(x, y, z)$ (in the dimensionless variables) simplify to

$$(5.3) \quad \mathcal{R}e(\mathbf{J}_s(x, y, z)) = \begin{bmatrix} \cos(L\pi x) \sin(L\pi y) \sin(L\pi z) \left(\frac{3\pi^2}{\mu L^2} - \pi\sigma - \varepsilon\omega^2 \right) \\ -\sin(L\pi x) \cos(L\pi y) \sin(L\pi z) \left(\frac{6\pi^2}{\mu L^2} + \pi\sigma - 2\varepsilon\omega^2 \right) \\ \sin(L\pi x) \sin(L\pi y) \cos(L\pi z) \left(\frac{3\pi^2}{\mu L^2} - \pi\sigma - \varepsilon\omega^2 \right) \end{bmatrix}$$

and

$$(5.4) \quad \mathcal{I}m(\mathbf{J}_s(x, y, z)) = \begin{bmatrix} \cos(L\pi x) \sin(L\pi y) \sin(L\pi z) (\sigma\omega - \pi\varepsilon\omega) \\ -\sin(L\pi x) \cos(L\pi y) \sin(L\pi z) (2\sigma\omega + \pi\varepsilon\omega) \\ \sin(L\pi x) \sin(L\pi y) \cos(L\pi z) (\sigma\omega - \pi\varepsilon\omega) \end{bmatrix}.$$

This gives the right sides of (3.3) through (3.6) as $\mu L^2 \mathcal{R}e(\mathbf{J}_s(x, y, z))$, $\mu L^2 \mathcal{I}m(\mathbf{J}_s(x, y, z))$, $L(\nabla \cdot \mathcal{R}e(\mathbf{J}_s(x, y, z)))$, and $L(\nabla \cdot \mathcal{I}m(\mathbf{J}_s(x, y, z)))$ respectively. Having nondimensionalized the problem, we discretize it on the unit cube domain $[0, 1]^3$.

To obtain a representative frequency for these experiments, we consider the realistic setting where we expect to take $\sigma = 10^{-8}$ over the “air” region of a geophysical problem. For such small values of σ , the negative shift by M_ϵ becomes significant, reflecting the propagating nature of high-frequency electromagnetic waves in air, in contrast to their diffusive behavior within the Earth. To determine a representative frequency here, we consider the standard requirement used in solving the acoustic Helmholtz equation of maintaining at least 10 points per wavelength (ppw) [13]. A straightforward calculation gives the frequency $f_0 = 9.5934 \times 10^6$ as that at which we achieve 10 ppw resolution for the related eddy-current wave equation with $\sigma = 10^{-8}$ on a 32^3 uniform mesh of the unit cube. Table 5.1 presents numerical results obtained taking conductivity $\sigma = 1.0$ over the entire domain and varying both the mesh size and the frequency. For this value of σ , the discrete problems remain definite for all of the meshes and frequencies considered in Table 5.1. Overall, we see only

TABLE 5.1
Solver performance with uniform mesh refinement for definite problems.

$f_0 = 9.5934 \times 10^6$, $\sigma = 1.0$ 16 ³ mesh: Matrix size = 71874, nnz per row = 42 32 ³ mesh: Matrix size = 549,250, nnz per row = 48 64 ³ mesh: Matrix size = 4,293,378, nnz per row = 52									
ppw	Mesh (N^3)	Freq.	Preconditioning-1			Preconditioning-2			
			Outer	Inner	CPU time	Outer	Inner	Innermost	
10	16 ³	$f_0/2$	3	58	3.03 s	3	58	208	3.08 s
	32 ³	f_0	3	62	25.07 s	3	62	224	26.42 s
	64 ³	$2f_0$	3	70	4 m 27.4 s	3	70	256	4 m 48.87 s
20	16 ³	$f_0/4$	3	64	3.08 s	3	64	232	3.07 s
	32 ³	$f_0/2$	3	70	26.86 s	3	70	256	28.35 s
	64 ³	f_0	3	82	4 m 49.84 s	3	82	304	5 m 8.64 s
40	16 ³	$f_0/8$	3	74	3.25 s	3	74	272	3.39 s
	32 ³	$f_0/4$	3	82	30.91 s	3	82	304	33.1 s
	64 ³	$f_0/2$	3	84	4 m 44.57 s	3	84	312	5 m 9 s

minor variations in performance in these results, with slight growth in inner iteration counts as we vary the mesh size at fixed resolution and (slightly surprisingly) as we increase the resolution from 10, to 20, and to 40 ppw on fixed meshes. The outer iterations recorded are *full block-LU preconditioned* FGMRES iterations up to reduction of the relative residual norm to 10^{-10} , while the inner iterations are block-diagonally AMS-preconditioned FGMRES iterations of the \mathcal{A}_{11} subsystem, up to a reduction of 10^{-9} . Here, solver performance with Preconditioning-1 is quite satisfactory and the use of Preconditioning-2 does not offer any improvements in the time-to-solution for these problems. With Preconditioning-2, *Innermost* iterations refer to the embedded AMS-preconditioned single-block curl-curl FGMRES wrapper iterations employed for reduction to a loose tolerance of 10^{-2} ; we see that multiple innermost iterations are required per inner iteration but that no improvement in inner (or outer) convergence is gained from this additional work. Table 5.1 shows that the solver behavior for definite problems is quite stable, and its performance is satisfactory (in terms of efficiency) under uniform mesh refinement. We note that these computations are sequential and, therefore, an increase in total CPU time by a factor of eight upon refinement represents optimal scaling.

To examine solver performance on problems that are indefinite, we consider problems with piecewise constant conductivity, σ , chosen to be 1 in part of the domain and 10^{-4} or 10^{-8} in the remainder, now on a fixed mesh of 32³. Table 5.2 presents numerical results for these problems, with outer and inner tolerances the same as for the definite problems. While the problem is quite challenging (due to its indefiniteness) when we use a small value of σ over the whole space, we see that reasonable performance is maintained when we keep $\sigma = 1$ over much of the computational domain. Already when only a single element's thickness has the lower conductivity value, as shown in the bottom line of Table 5.2, we see notable degradation in comparison to the results in Table 5.1. However, the deterioration in performance with increasing portion of the domain at lower conductivity value is not too drastic until we reach the point where half of the domain has the lower value. While the use of inner Krylov acceleration within Preconditioning-2 is natural here, we find that while this lowers the outer and inner iteration counts, it comes at the expense of a large number of

TABLE 5.2

Solver performance for problems on 32^3 uniform mesh with various levels of indefiniteness.

$f_0 = 9.5934 \times 10^6$, $\sigma \in \{10^{-8}, 10^{-4}\}$ 32^3 mesh: matrix size = 549,250, nnz per row = 48						
Space with $\sigma \in \{10^{-8}, 10^{-4}\}$	$\sigma = 10^{-8}$			$\sigma = 10^{-4}$		
	Outer	Inner	CPU time	Outer	Inner	CPU time
Full	3	10957	5h 23m 5.7s	3	3107	54m 57.65s
Half	6	11706	3h 30m 9.9s	5	2906	35m 17.99s
Quarter	3	2630	30m 29.95s	4	1384	12m 40.35s
8th part	4	1249	10m 18.8s	5	808	6m 10.64s
32nd part	4	1259	9m 48.29s	3	448	3m 15.97s

innermost iterations and, consequently, results in an overall increase in CPU time. Thus, we find that Preconditioning-1 is more effective for these problems on uniform meshes. We also note that, for these indefinite problems, delayed convergence seems to stem from the underlying core algorithms, particularly the AMS preconditioner that is intended for semidefinite problems. It is clear that work to improve AMS (or other preconditioner) performance in the indefinite case could directly benefit performance here.

5.2. Geophysical model problems. The three model problems considered here are distinguished by (1) the size of the physical domain associated with the model, and the particular locally refined mesh employed, (2) the conductivity contrast across the model, and (3) the forcing term included in the PDE. We include two field-scale examples, one of simplistic construction (the prism-wire problem) and one of a more realistic setting (modeling the Voisey's Bay ovoid ore deposit), and one lab-scale experiment (the cube-in-brine problem).

5.2.1. The prism-wire problem. This problem models a $40 \times 40 \times 40$ km domain of interest, typical of realistic geophysical surveys. The z -axis is split around the plane $z = 0$, which represents the air-ground interface, with positive z representing the air region of height 20 km. A conductive prism of dimension $120 \times 200 \times 400$ meters is placed 100 meters beneath the surface and excited with a wire of length 100 meters placed on the air-ground interface, 1 km away from the prism (in the x -direction). The frequency for this experiment was set at 3 Hz. From a geophysical perspective—which includes the geometry, the source type, conductivity contrast due to the background medium, and the rather low frequency—this example is almost completely galvanic [5]. A tetrahedral mesh of the domain is generated using the TetGen library [51, 52], refined in the region of the prism and highly refined around the grounded wire source. A portion of the cross section of this model is shown in Figure 5.1.

To represent the essentially one-dimensional wire source, we use a step function with finite support. Along the positive x -axis, we define a cylinder with fixed radius r chosen to be between 0.5 meters and 1 meter, depending on the specific mesh under consideration. The PDE source is, then, taken to be the constant value $\frac{1}{2\pi r}$ within this cylinder, for $0 < x < 100$ meters and zero outside. The choice of r is made small enough to accurately approximate the delta function used in [5] but large enough so that the source is *visible* on a given mesh. The conductivity, σ , is piecewise constant; in the air region, its value is 10^{-8} Siemens/meter (S/m). In the ground, but excluding

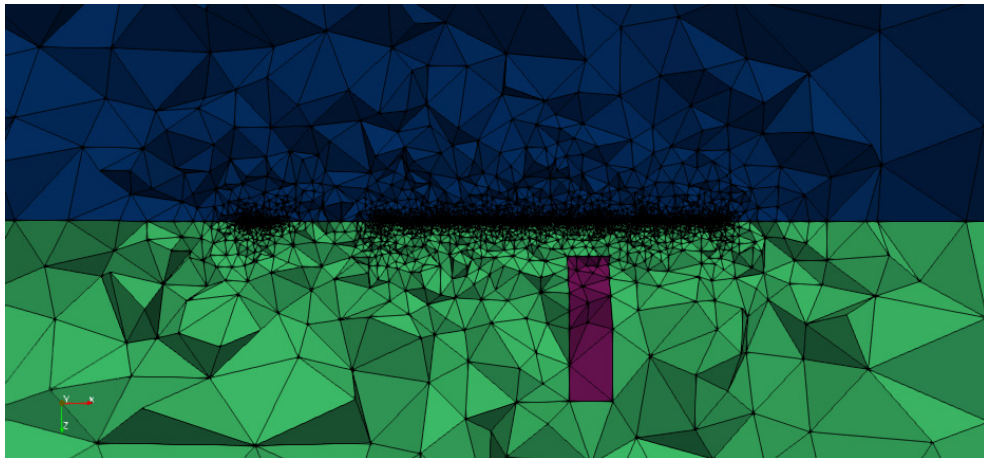


FIG. 5.1. A selected portion of the xz -cross section of the prism-wire model along the central plane.

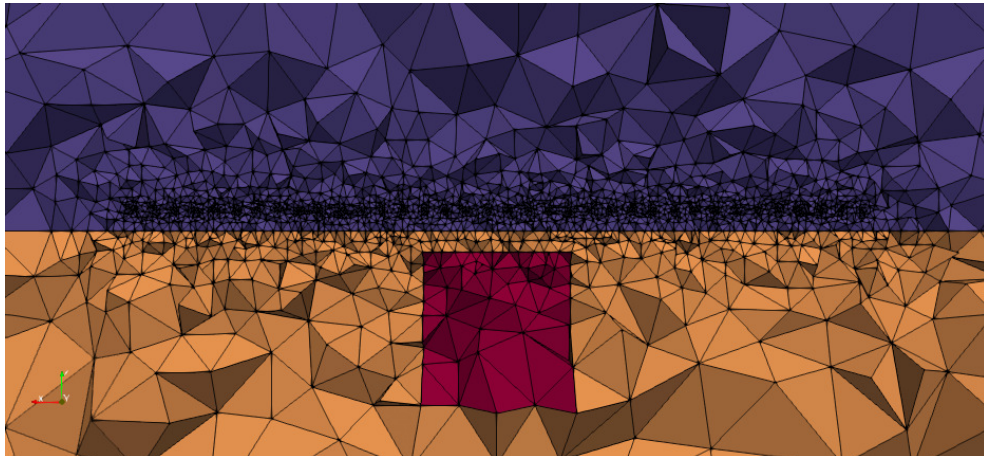


FIG. 5.2. A selected portion of the xz -cross section of the cube-in-brine model along the central plane.

the region where the prism is placed, it is 0.02 S/m . In the conductive prism, it is 0.2 S/m .

5.2.2. The cube-in-brine problem. This problem represents a physical-scale model (i.e., laboratory-scale experiment) where the *inductive* component of the solution is dominant. Here, the domain is a $40 \times 40 \times 40 \text{ cm}$ cube, with the top 20 cm representing the air region. Below the plane $z = 0$ is a brine tank containing a highly conductive graphite cube of dimension $14 \times 14 \times 14 \text{ cm}$ whose top plane is held 2 cm below the brine surface. A magnetic dipole source is used for excitation, and the transmitter-receiver pair is situated 2 cm above the brine surface. Figure 5.2 illustrates the model.

The magnetic dipole source (point charge) is again modeled using a step function, now with spherical support with radius $r = 1 \text{ cm}$, centered at physical coordinates

(0, 0, 2) cm, and value $\frac{1}{(4/3)\pi r^3}$. Again, this radius is chosen so that the source is clearly represented on the mesh. The conductivity σ is taken to be 63000 S/m for the graphite cube, 7.3 S/m for brine, and 10^{-8} for air. While the brine and cube conductivities are much greater than those in the field-scale models considered here, they are chosen based on the principles of physical-scale modeling, so that the physical response is meaningful. In order to fully realize this, much greater frequencies will be used in this model than in the two field-scale models. Note, however, that the air conductivity does not change in this modeling regime, making a larger contrast than the other models that makes solution of the resulting discretized equations more difficult. The complete details of this model are available in [23].

5.2.3. The Voisey's Bay ovoid problem. The final example considered here is based on an idealized model of the real-world ore body found near Voisey's Bay in Labrador, Canada, where a huge ovoid-shaped sulphide lens makes up a nickel-copper-cobalt deposit. The details of the deposit are discussed in [12], which reports an elongated body buried roughly 20 meters beneath Earth's surface. In [5], physical parameters were chosen through trial and error to closely match recorded field data, due to the unavailability of true physical properties. We use these values here, with conductivity equal to 100 S/m for the ovoid lens, 0.001 S/m for the surrounding mineral deposit, and 10^{-8} for air.

Figure 5.3 shows a portion of the cross section of this model. The mesh is refined along the source, as well as in the ore region. Coordinates of the physical terrain are *Easting* 555200–556400, *Northing* 6242800–6243400, and *Depth* –200–200 meters. The dipole source is approximately over the center of the ovoid situated at the coordinates (555837.5, 6243201, 110) meters.

5.3. Numerical experiments and observations. In this section, we explore the performance of the proposed preconditioning framework for the three model problems described above. As usual, we primarily focus on two metrics of performance, the number of preconditioned (outer) Krylov iterations and total CPU time-to-solution. An important distinction here, however, is that it is naturally possible to minimize

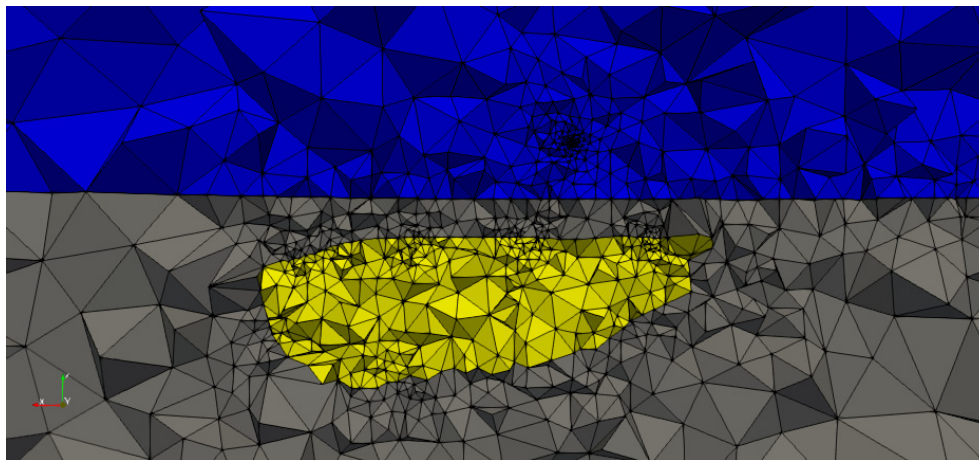


FIG. 5.3. A selected portion of the vertical cross section of the Voisey's Bay ovoid model approximately along a plane through the center of the ore.

the number of outer Krylov iterations at the expense of CPU time, by performing many inner iterations, to solve the component blocks. Here, we explore the trade-off between outer and inner iterations with the goal of minimizing CPU time-to-solution.

As mentioned in section 4.4, we compare results for the preconditioning framework between two approaches that differ only in the way that AMS is used within the *curl-curl* solver as illustrated in Algorithm 4.1. In the first approach, we directly precondition FGMRES for solving the subsystem involving \mathcal{A}_{11} with a single cycle of AMS applied to each diagonal block of $\tilde{\mathcal{A}}_{11}$, denoted as Preconditioning-1. In the second approach, denoted as Preconditioning-2, the diagonal blocks of $\tilde{\mathcal{A}}_{11}$ are inverted through AMS-preconditioned FGMRES. These innermost iterations are done to low tolerance, such as a relative reduction in residual norm by a factor of 10^{-1} or 10^{-2} , requiring only a few (up to four) iterations of AMS-preconditioned FGMRES to achieve the reduction required. We note that FGMRES is used here in place of CG as the operator \mathcal{A}_{11} , as well as its idealized preconditioning operator $\tilde{\mathcal{A}}_{11}$ (to which AMS is applied) are mildly indefinite and, therefore, FGMRES seems better suited for these problems. As will be shown, both strategies are effective.

5.3.1. Numerical results with Preconditioning-1. Here, we present detailed information on the outer FGMRES convergence, along with diagnostics of the performance of the inner solvers. An important comparison is of the effects of the choices of tolerances for the inner solvers (both for \mathcal{A}_{11} and the Schur complement) on the efficiency of the outer iterations. In this section, we fix the meshes on which each problem is discretized, leading to the algebraic properties of the discretization matrices shown in Table 5.3. We note that while the cube-in-brine problem is given on the smallest mesh, due to the physical-scale modeling assumptions, it is also associated with the highest frequencies of the source term. This makes this problem substantially more difficult to solve in many cases than the other two examples, even though they are substantially larger.

Table 5.4 shows the convergence of Preconditioning-1 for the prism-wire problem with “strict” inner tolerances of relative residual reduction by a factor of 10^{-12} for the curl-curl systems and 10^{-10} for the Schur complement block. This experiment is run at a frequency of 3 Hz and, as such, the ideal block-diagonal preconditioner, $\tilde{\mathcal{A}}_{11}$, constructed for preconditioning of \mathcal{A}_{11} remains positive-definite. Consequently, the outer preconditioner performs quite well, requiring only 4 iterations to achieve a relative reduction in the residual norm by a factor of 10^{-12} . Importantly, the inner preconditioners also perform well here, with the two $\hat{\mathcal{A}}_{11}$ -preconditioned solves for \mathcal{A}_{11} requiring no more than 40 total inner iterations per outer iteration, and fewer than 20 AMG iterations on the Schur complement, \mathcal{S} , per outer iteration. Despite the relatively “expensive” cost of the AMS preconditioner, the total time solution (in serial) using these parameters is less than 15 minutes.

TABLE 5.3
Algebraic characteristics of the three model problems.

Problem	Matrix sizes	No. of nonzeros	nnz/row
Prism-wire	2,651,894	152,145,474	57.37
Cube-in-brine	246,062	14,040,248	57.06
Ovoid	2,297,466	131,912,590	57.41

TABLE 5.4
Convergence pattern of prism-wire problem with strict inner tolerances.

Prism-wire problem			Inner curl-curl tol = 1e-12 AMG tol = 1E-10
Outer iter. no.	Residual norm	Number of precond. inner Krylov solves	No. of AMG cycles for scalar solves
0	1.34311e-05		
1	1.55251e-09	40	18
2	5.43616e-12	32	14
3	1.19025e-14	24	14
4	3.05933e-17	25	14
Total CPU time (entire solve) = 13m30s			
Total no. of inner iterations = 121			
Total no. of AMS cycles (for prec. curl-curl solves) = 242			
Total no. of AMG cycles (scalar solves) = 60			

TABLE 5.5
Convergence pattern of the solver for the prism-wire problem with lax inner tolerances.

Prism wire problem			Inner curl-curl tol = 1E-5 AMG tol = 1E-6
Outer iter. no.	Residual norm	Number of precond. inner Krylov solves	No. of AMG cycles for scalar solves
0	1.34311e-05		
1	5.79967e-08	8	10
2	1.29434e-09	24	10
3	1.62048e-11	16	9
4	3.99044e-14	16	10
5	1.76113e-16	22	10
6	8.89608e-19	18	10
Total CPU time (entire solve) = 11m6s (sec)			
Total no. of inner iterations = 104			
Total no. of AMS cycles (for prec. curl-curl solves) = 208			
Total no. of AMG cycles (scalar solves) = 59			

For contrast, Table 5.5 presents data on the convergence for the same problem, now using relatively lax inner tolerances of relative reduction of the residual norm by 10^{-5} for the \mathcal{A}_{11} subsystems and 10^{-6} for the Schur complement. As expected, this leads to a moderate increase in the number of outer iterations needed to achieve the same reduction in the overall residual norm, from four to six. This is compensated for by a marginal drop in the total number of inner iterations required for the \mathcal{A}_{11} subsystem, by 14% from 121 to 104, with almost no change in the number of AMG iterations to solve the Schur complement. As a result, the total time-to-solution drops by 18%, demonstrating that the bulk of the CPU does, indeed, come from the AMS preconditioning step. As the experiments below will show, this improvement in time-to-solution with weaker inner tolerances is, unfortunately, not universal, suggesting that either problem-by-problem experimentation is needed to determine “optimal” inner tolerances or that stronger inner tolerances should be used to ensure acceptable performance. We also observe that these results offer a noticeable improvement over those reported in [5] for nearly identical problems, using ILUT-preconditioned FGMRES as the solver.

Tables 5.6 and 5.7 present similar experiments for the Ovoid problem, now with a frequency of 900 Hz to match that of the data collected during an actual helicopter

TABLE 5.6
Convergence pattern of Voisey's Bay ovoid problem with strict inner tolerances.

Ovoid problem			Inner curl-curl tol = 1E-12 AMG tol = 1e-10
Outer iter. no.	Residual norm	Number of precond. inner Krylov solves	No. of AMG cycles for scalar solves
0	1.59778		
1	0.00295485	86	15
2	7.34092e-08	83	15
3	9.9355e-13	106	15
Total CPU time (entire solve) = 19m38s			
Total no. of inner iterations = 275			
Total no. of AMS cycles (for prec. curl-curl solves) = 550			
Total no. of AMG cycles (scalar solves) = 45			

TABLE 5.7
Convergence pattern of Voisey's Bay ovoid problem with lax inner tolerances.

Ovoid problem			Inner curl-curl tol = 1E-10 AMG tol = 1e-8
Outer iter. no.	Residual norm	Number of precond. inner Krylov solves	No. of AMG cycles for scalar solves
0	1.59778		
1	0.00317403	76	11
2	1.98665e-07	80	10
3	3.02697e-11	98	11
4	1.53358e-15	98	11
Total CPU-time (entire solve) = 22m46s			
Total no. of inner iterations = 352			
Total no. of AMS cycles (for prec. curl-curl solves) = 704			
Total no. of AMG cycles (scalar solves) = 43			

survey of the region [12, 25]. At this higher frequency (and with the higher contrast in conductivities) in this example, we see somewhat degraded performance, particularly in the inner iterations. This is not surprising as the shifted curl-curl matrices used in the solver for the \mathcal{A}_{11} subsystem are now indefinite, due to the higher frequency. Consequently, we now see that the use of stricter tolerances in Table 5.6 leads to the more efficient solver in comparison to the slightly looser tolerances in Table 5.7, while further degradation in time-to-solution is seen with even weaker inner solves. While AMG on the Schur complement system performs similarly to the prism-wire case, not enough improvement in the inner iterations for the curl-curl subblock are seen to overcome the cost of the increased number of outer iterations.

For the cube-in-brine problem, we consider two different frequencies, one relatively low, 4 kHz, and one higher frequency, 400 kHz, both corresponding to those used in experiments in [21, 23]. Figure 5.4 provides data for the low-frequency experiment, with the inner convergence tolerance for AMG fixed at a relative reduction in residual norm by a factor of 10^{-10} and varying values for the inner convergence tolerance for the \mathcal{A}_{11} subsystem. Figure 5.5 provides corresponding experiments for the higher-frequency experiment. At 4 kHz, we see convergence behavior qualitatively similar to that of the prism-wire problem, with overall savings in total time-to-solution as the inner tolerance on the \mathcal{A}_{11} subsystem is relaxed, due to a reduction in total number of inner AMS iterations, even with an increase in both inner AMG iterations

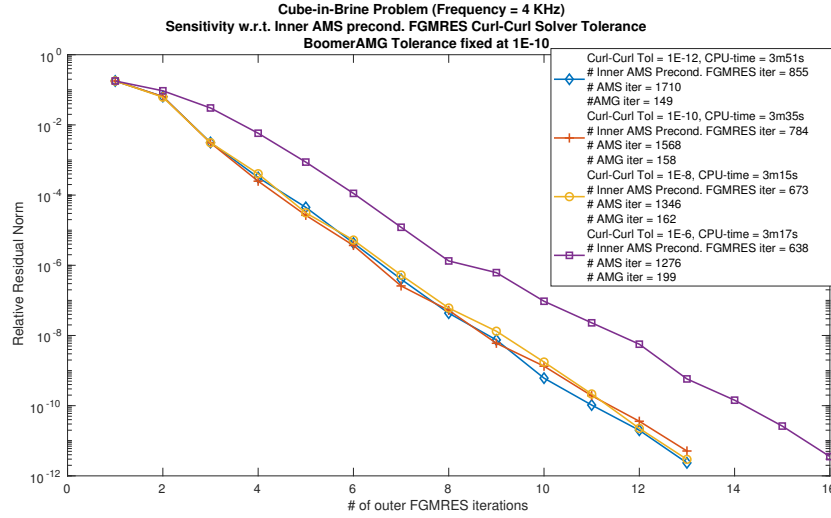


FIG. 5.4. *Cube-in-brine problem (low-frequency).* Convergence history of the outer Krylov method. Relative residual is measured in the discrete L_2 norm.

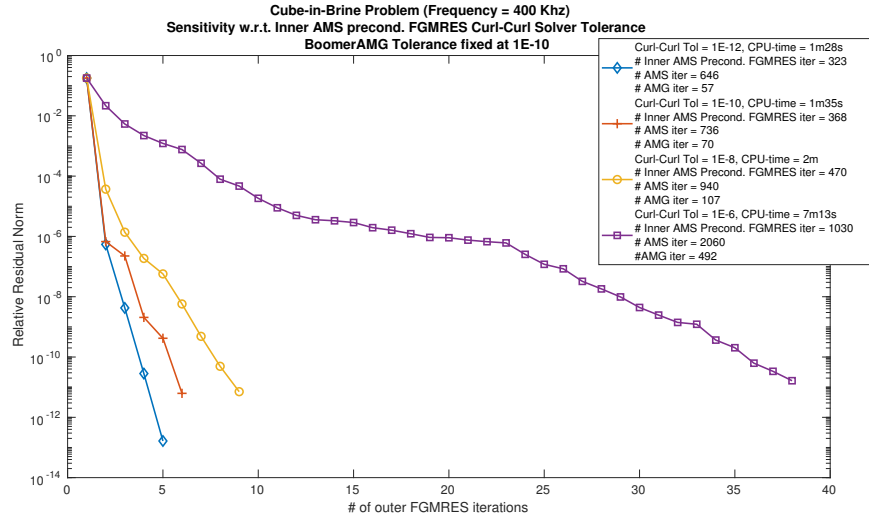


FIG. 5.5. *Cube-in-brine problem (high-frequency).* Convergence history of the outer Krylov method. Relative residual is measured in the discrete L_2 norm.

and outer iterations. In contrast, at 400 kHz, we see growth in the total number of AMS iterations needed for convergence as the inner tolerance on the \mathcal{A}_{11} subsystem is relaxed, as the decrease in number of AMS iterations needed per outer iteration is not sufficient to balance the increase in number of outer iterations required. Balancing these two behaviors is, again, difficult, but it is noteworthy that the decrease in cost in the low-frequency case is quite moderate, while the increase in cost in the high-frequency case is quite substantial; thus, it seems reasonable to use relatively strict tolerances to ensure reasonable behavior of the preconditioner in such settings.

5.3.2. Numerical results with Preconditioning-2. Overall, there seems to be little benefit to be expected in further improvements in the preconditioner for the prism-wire problem. Thus, in this section, we focus on the other two problems and explore if more robust performance can be achieved through tuning of the innermost iterations in the preconditioner. Here, we use refined meshes that are again non-uniform and include regions of saturation and stretching. These meshes are generated using the TetGen software [51, 52], with a *higher quality* setting for the output mesh, constructed with either a smaller bound on the aspect ratio or larger bound on the minimum dihedral angle. In this section, meshes were determined with the bound on the aspect ratio set to 1.02, to obtain a very fine mesh consistent with the saturation and stretching of the mesh topology necessary to accurately model the geophysical experiments considered here. The resulting linear system for the ovoid problem has 6,211,156 degrees of freedom and an average of 58 nonzero entries per row of the matrix, while that for the cube-in-brine example has 3,768,046 degrees of freedom and an average of 62 nonzero entries per row of the matrix. We solve both problems to a relative reduction in the residual norm by a factor of 10^{-10} .

Table 5.8 presents results for the solution of the Voisey's Bay ovoid model on the refined mesh with variations in the conductivity, σ , chosen within the ovoid lens region, still for frequency 900 Hz. While there is clearly some variation in performance with changes in this conductivity, overall the performance is rather insensitive to its value. For any fixed problem (choice of σ), we see improvement in time-to-solution (sometimes significantly) when using stronger inner convergence tolerances (right side of the table). Whether using strong or weak inner tolerances, we mostly see benefits in using the Preconditioning-2 strategy, including an "innermost" layer of preconditioned FGMRES on the solution of the subblocks of the \mathcal{A}_{11} subsystem with associated relative residual norm reduction tolerance of 10^{-1} . When that tolerance is further reduced to 10^{-2} , outer iteration counts don't improve, and total time-to-solution increases. We note, nonetheless, that in two of the three cases considered, Preconditioning-1 outperforms Preconditioning-2 by several minutes of CPU time, but that the Preconditioning-2 strategy, with stricter inner tolerances and 10^{-1} innermost tolerance, offers very steady time-to-solution, varying by only a few minutes over the three cases.

Table 5.9 details performance for the cube-in-brine problem on the refined mesh at frequencies of 4, 10, 40, 100, and 400 kHz, again corresponding to those used in experiments in [21, 23]. Here, results are more mixed. At 10, 40, and 100 kHz, there seems to be a clear advantage to again using strong inner convergence tolerances, with savings of up to a factor of two in solve times possible. At 4 and 400 kHz, however, the overall performance between the two choices of inner tolerances is quite comparable. For a fixed frequency and set of inner tolerances, we generally see that the stricter

TABLE 5.8

Results for Voisey's Bay ovoid problem on refined mesh for three different conductivity values in the region of the ovoid lens.

σ in ovoid	curl-curl solver tol = 10^{-8} , AMG tol = 10^{-8}		curl-curl solver TOL = 10^{-12} , AMG tol = 10^{-10}		
	Preconditioning-1		Preconditioning-2		Preconditioning-1
	Plain AMS	FGMRES-AMS tol = 10^{-2}	Plain AMS	FGMRES-AMS tol = 10^{-2}	FGMRES-AMS tol = 10^{-1}
2 S/m	5 / 1h42m36s	4 / 1h43m11s	4 / 1h38m48s	2 / 1h14m29s	2 / 1h41m14s
100 S/m	5 / 2h3m24s	4 / 2h2m31s	4 / 1h49m33s	3 / 1h50m	2 / 1h46m29s
500 S/m	6 / 2h10m35s	5 / 2h20m39s	5 / 2h2m	2 / 1h21m59s	2 / 1h48m47s
					2 / 1h24m22s

TABLE 5.9
Results for the cube-in-brine problem on refined mesh for a range of frequencies.

Freq. (Hz)	curl-curl solver tol = 10^{-8} , AMG tol = 10^{-8}			curl-curl solver tol = 10^{-12} , AMG tol = 10^{-10}				
	Preconditioning-1		Preconditioning-2		Preconditioning-1		Preconditioning-2	
	Plain AMS	FGMRES-AMS tol = 10^{-2}	FGMRES-AMS tol = 10^{-1}	Plain AMS	FGMRES-AMS tol = 10^{-2}	FGMRES-AMS tol = 10^{-1}		
4000	6 / 1h1m18s	6 / 1h50m5s	6 / 1h16m30s	6 / 1h8m47s	6 / 1h40m15s	6 / 1h19m13s		
10000	7 / 1h6m5s	6 / 1h23m25s	7 / 1h23m46s	4 / 54m41s	3 / 53m7s	4 / 57m15s		
40000	17 / 2h28m	8 / 1h42m31s	9 / 1h41m9s	4 / 50m38s	4 / 59m29s	4 / 56m3s		
100000	22 / 2h51m36s	22 / 4h21m13s	10 / 1h20m53s	5 / 43m45s	5 / 59m32s	6 / 1h4m52s		
400000	21 / 2h26m13s	17 / 2h46m48s	13 / 1h45m56s	14 / 2h6m33s	10 / 2h39m	11 / 1h53m25s		

innermost tolerance of 10^{-2} leads to an increase in CPU time-to-solution over that of 10^{-1} , sometimes substantially, but not always. However, this improvement, when present, is never by more than a few minutes in a computation time of about an hour. Comparing, then, performance between Preconditioning-1 and Preconditioning-2 with innermost tolerance of 10^{-1} , with Preconditioning-2 offering faster time-to-solution for frequencies 10 kHz and higher for the loose inner tolerances, but only for the highest frequency, 400 kHz, for the stricter inner tolerances. In some cases, the improvement offered by one strategy or the other is substantial, with Preconditioning-1 being about 1/3 faster at 100 kHz with stricter inner tolerances; however, in many cases, the differences are on the scale of only a few minutes.

6. Conclusions and outlook. In this paper, we have presented a preconditioning framework for the block 4×4 matrices arising from FEM discretization of an implicitly gauged formulation of Maxwell's equations in the regime of geophysical imaging. The iterative solution of this system is very challenging, and past attempts at using general-purpose preconditioners, such as ILUT, have given quite poor results. A combination of factors contribute to this, including the general difficulties with solution of Nédélec discretizations, jumps in material properties, and indefiniteness due to inclusion of the second-order derivative in time that becomes important at high frequencies.

While block-diagonal and block-triangular preconditioners are ineffective for this problem, we propose an approximate *LU* factorization based on a continuum representation of the Schur complement. Furthermore, we present an approach for the approximate inversion of the *LU* factors, using the Hiptmair–Xu framework as implemented in the auxiliary-space Maxwell solver in Hypre [31, 36]. The proposed framework is tested with three model problems, with greatly improved results over those existing in the literature. Particular attention is paid to the interaction between inner and outer iterations used to define the preconditioner, and finding an effective parameter choice to balance the costs of the nested iterations. Future work includes the application of this preconditioning framework in the context of real-world geophysical inversion, where a range of frequencies and conductivity structures must be considered, and extending it to the larger, 6×6 , block structure that arises when the gauge condition is implemented via a Lagrange multiplier, as in [5]. Finally, we note that any improvements in preconditioner performance for the vector Helmholtz equation (either in Maxwell form or for the vector Laplacian) could be leveraged to improve the solvers considered here, by improving performance of the underlying auxiliary-space preconditioner. Of particular importance is the fact that the convergence of AMS for indefinite operators is not well-understood; extending AMS and its analysis to include this case is clearly worth further investigation.

Acknowledgments. We extend our thanks to Patrick Farrell, Tzanio Kolev, Domenico Lahaye, and Raphael Roehlitz for insightful discussions and support of the free software libraries that were used in this work. We also thank the anonymous referees for their helpful comments that greatly improved the presentation within this manuscript.

REFERENCES

- [1] *High Performance Preconditioners*, <http://www.llnl.gov/CASC/hypre>.
- [2] *MFEM: Modular Finite Element Methods Library*, <https://doi.org/10.11578/dc.20171025.1248>.
- [3] M. S. ALNÆS, J. BLECHTA, J. HAKE, A. JOHANSSON, B. KEHLET, A. LOGG, C. RICHARDSON, J. RING, M. E. ROGNES, AND G. N. WELLS, *The FEniCS project version 1.5*, Arch. Numer. Software, 3 (2015), <https://doi.org/10.11588/ans.2015.100.20553>.
- [4] S. ANSARI AND C. G. FARQUHARSON, *Three dimensional finite element numerical modeling of geophysical electromagnetic data using vector and scalar potentials and unstructured grids*, Geophysics, 79 (2014), pp. E149–E165.
- [5] S. ANSARI, C. G. FARQUHARSON, AND S. MACLACHLAN, *A gauged finite-element potential formulation for accurate inductive and galvanic modelling of three-dimensional electromagnetic problems*, Geophys. J. Internat., 210 (2017), pp. 105–129.
- [6] D. ARNOLD, R. FALK, AND R. WINTHER, *Multigrid in $H(\text{div})$ and $H(\text{curl})$* , Numer. Math., 85 (2000), pp. 197–217.
- [7] S. R. ARRIDGE, H. EGGER, AND M. SCHLOTTBOM, *Preconditioning of complex symmetric linear systems with applications in optical tomography*, Appl. Numer. Math., 74 (2013), pp. 35–48, <https://doi.org/10.1016/j.apnum.2013.06.008>.
- [8] D. V. AVDEEV, *Three-dimensional electromagnetic modelling and inversion from theory to practice*, Surv. Geophys., 26 (2005), pp. 767–799.
- [9] O. AXELSSON, M. NEYTCHEVA, AND B. AHMAD, *A comparison of iterative methods to solve complex valued linear algebraic systems*, Numer. Algorithms, 66 (2014), pp. 811–841, <https://doi.org/10.1007/s11075-013-9764-1>.
- [10] A. H. BAKER, R. D. FALGOUT, T. V. KOLEV, AND U. M. YANG, *Multigrid smoothers for ultraparallel computing*, SIAM J. Sci. Comput., 33 (2011), pp. 2864–2887, <https://doi.org/10.1137/100798806>.
- [11] S. BALAY, S. ABHYANKAR, M. F. ADAMS, J. BROWN, P. BRUNE, K. BUSCHELMAN, L. DALCIN, V. EIJKHOUT, W. D. GROPP, D. KAUSHIK, M. G. KNEPLEY, D. A. MAY, L. C. MCINNES, R. T. MILLS, T. MUNSON, K. RUPP, P. SANAN, B. F. SMITH, S. ZAMPINI, H. ZHANG, AND H. ZHANG, *PETSc Users Manual*, Tech. Report ANL-95/11, Revision 3.9, Argonne National Laboratory, 2018, <http://www.mcs.anl.gov/petsc>.
- [12] S. J. BALCH, *Ni-Cu sulphide deposits with examples from Voisey's Bay*, in *Geophysics in Mineral Exploration: Fundamentals and Case Histories*, C. Lowe, M. D. Thomas, and W. A. Morris, eds., Geological Association of Canada, 1999.
- [13] A. BAYLISS, C. I. GOLDSTEIN, AND E. TURKEL, *On accuracy conditions for the numerical computation of waves*, J. Comput. Phys., 59 (1985), pp. 396–404.
- [14] M. BENZI AND D. BERTACCINI, *Block preconditioning of real-valued iterative algorithms for complex linear systems*, IMA J. Numer. Anal., 28 (2008), pp. 598–618, <https://doi.org/10.1093/imanum/drm039>.
- [15] D. V. BOERNER, *Numerical modelling in geo-electromagnetics: Advances and challenges*, Surv. Geophys., 31 (2010), pp. 225–245.
- [16] D. BRAESS, *Finite Elements*, 2nd ed., Cambridge University Press, Cambridge, UK, 2001.
- [17] S. BRENNER AND L. SCOTT, *The Mathematical Theory of Finite Element Methods*, Texts in Appl. Math. 15, Springer-Verlag, New York, 1994.
- [18] M. CHANAUD, L. GIRAUD, D. GOUDIN, J. J. PESQUÉ, AND J. ROMAN, *A parallel full geometric multigrid solver for time harmonic Maxwell problems*, SIAM J. Sci. Comput., 36 (2014), pp. C119–C138, <https://doi.org/10.1137/130909512>.
- [19] S. CONSTABLE, *Ten years of marine CSEM for hydrocarbon exploration*, Geophysics, 75 (2010), pp. 75A67–75A81.
- [20] D. DAY AND M. A. HEROUX, *Solving complex-valued linear systems via equivalent real formulations*, SIAM J. Sci. Comput., 23 (2001), pp. 480–498.
- [21] K. DUCKWORTH, T. D. NICHOLS, AND E. S. KREBES, *Examination of the relative influence of current gathering on fixed loop and moving source electromagnetic surveys*, Geophysics, 66 (2001), pp. 1059–1066, <https://doi.org/10.1190/1.1487053>.

- [22] H. ELMAN, D. SILVESTER, AND A. WATHEN, *Finite elements and fast iterative solvers: With applications in incompressible fluid dynamics*, Numer. Math. Sci. Comput., Oxford University Press, New York, 2005.
- [23] C. G. FARQUHARSON, K. DUCKWORTH, AND D. W. OLDENBURG, *Comparison of integral equation and physical scale modeling of the electromagnetic responses of models with large conductivity contrasts*, Geophysics, 71 (2006), pp. G169–G177, <https://doi.org/10.1190/1.2210847>.
- [24] C. G. FARQUHARSON AND M. P. MIENSOPUST, *Three-dimensional finite element modelling of magnetotelluric data with a divergence correction*, J. Appl. Geophys., 75 (2011), pp. 699–710, <https://doi.org/10.1016/j.jappgeo.2011.09.025>.
- [25] D. G. GARRIE, *Digham Survey for Diamond Fields Resources Inc. Archean Resources Ltd. Voiseys Bay, Labrador*, Survey Report 1202, CGG Canada, 1995.
- [26] P. GHYSELS, X. S. LI, F.-H. ROUET, S. WILLIAMS, AND A. NAPOV, *An efficient multicore implementation of a novel HSS-structured multifrontal solver using randomized sampling*, SIAM J. Sci. Comput., 38 (2016), pp. S358–S384, <https://doi.org/10.1137/15M1010117>.
- [27] F. S. GRANT AND G. F. WEST, *Interpretation Theory in Applied Geophysics*, McGraw-Hill, New York, 1965.
- [28] A. V. GRAYVER AND M. BÜRG, *Robust and scalable 3-D geo-electromagnetic modelling approach using the finite element method*, Geophys. J. Internat., 198 (2014), pp. 110–125, <https://doi.org/10.1093/gji/ggu119>.
- [29] A. V. GRAYVER AND T. V. KOLEV, *Large-scale 3D geoelectromagnetic modeling using parallel adaptive high-order finite element method*, Geophysics, 80 (2015), pp. E277–E291.
- [30] R. HIPTMAIR, *Multigrid method for Maxwell's equations*, SIAM J. Numer. Anal., 36 (1999), pp. 204–225.
- [31] R. HIPTMAIR AND J. XU, *Nodal auxiliary space preconditioning in $H(\text{curl})$ and $H(\text{div})$ spaces*, SIAM J. Numer. Anal., 45 (2007), pp. 2483–2509, <https://doi.org/10.1137/060660588>.
- [32] P. B. HOOGHIEMSTRA, D. R. VAN DER HEUL, AND C. VUIK, *Application of the shifted-Laplace preconditioner for iterative solution of a higher order finite element discretisation of the vector wave equation: First experiences*, Appl. Numer. Math., 60 (2010), pp. 1157–1170, <https://doi.org/10.1016/j.apnum.2010.07.004>.
- [33] J. HU, R. TUMINARO, P. BOCHEV, C. GARASI, AND A. ROBINSON, *Toward an h -independent algebraic multigrid method for Maxwell's equations*, SIAM J. Sci. Comput., 27 (2006), pp. 1669–1688, <https://doi.org/10.1137/040608118>.
- [34] H. JAHANDARI AND C. G. FARQUHARSON, *Finite-volume modelling of geophysical electromagnetic data on unstructured grids using potentials*, Geophys. J. Internat., 202 (2015), pp. 1859–1876.
- [35] J. JIN, *The Finite Element Method in Electromagnetics*, 3rd ed., Wiley, New York, 2014.
- [36] T. V. KOLEV AND P. VASSILEVSKI, *Parallel auxiliary space AMG for $H(\text{curl})$ problems*, J. Comput. Math., 27 (2009), pp. 604–623, <https://doi.org/10.4208/jcm.2009.27.5.013>.
- [37] D. LAHAYE, H. DE GERSEM, S. VANDEWALLE, AND K. HAMEYER, *Algebraic multigrid for complex symmetric systems*, IEEE Trans. Magn., 36 (2000), pp. 1535–1538.
- [38] A. LOGG, K. B. OELGAARD, M. E. ROGNES, AND G. N. WELLS, *FFC: The FEniCS form compiler*, in *Automated Solution of Differential Equations by the Finite Element Method*, Lect. Notes Comput. Sci. Eng. 84, A. Logg, K.-A. Mardal, and G. N. Wells, eds., Springer, New York, 2012, pp. 227–238.
- [39] A. LOGG, G. N. WELLS, AND J. HAKE, *DOLFIN: A C++/python finite element library*, in *Automated Solution of Differential Equations by the Finite Element Method*, Lect. Notes Comput. Sci. Eng. 84, A. Logg, K.-A. Mardal, and G. N. Wells, eds., Springer, 2012, pp. 175–224.
- [40] D. LOGHIN AND A. J. WATHEN, *Schur complement preconditioning for elliptic systems of partial differential equations*, Numer. Linear Algebra Appl., 10 (2003), pp. 423–443, <https://doi.org/10.1002/nla.322>.
- [41] S. P. MACLACHLAN AND C. W. OOSTERLEE, *Algebraic multigrid solvers for complex-valued matrices*, SIAM J. Sci. Comput., 30 (2008), pp. 1548–1571.
- [42] K.-A. MARDAL AND R. WINTHER, *Preconditioning discretizations of systems of partial differential equations*, Numer. Linear Algebra Appl., 18 (2011), pp. 1–40, <https://doi.org/10.1002/nla.716>.
- [43] L. MARIONI, J. R. ALVES Z., E. HACHEM, AND F. BAY, *A new approach to solve complex valued systems arising from the solution of Maxwell equations in the frequency domain through real-equivalent formulations*, Numer. Linear Algebra Appl., 24 (2017), e2079, <https://doi.org/10.1002/nla.2079>.
- [44] P. MONK, *Finite-Element Methods for Maxwell's Equations*, Oxford University Press, New York, 2003.

- [45] M. F. MURPHY, G. H. GOLUB, AND A. J. WATHEN, *A note on preconditioning for indefinite linear systems*, SIAM J. Sci. Comput., 21 (2000), pp. 1969–1972.
- [46] M. NABIGHIAN, *Comment on "Electromagnetic geophysics: Notes from the past and the road ahead"* (Michael S. Zhdanov, 2010: *Geophysics*, 75 (5), 75A49–75A66), *Geophysics*, 77 (2012), pp. X3–X10.
- [47] J. C. NÉDÉLEC, *Mixed finite element in R^3* , Numer. Math., 35 (1980), pp. 315–341.
- [48] G. A. NEWMAN, *A review of high-performance computational strategies for modeling and imaging of electromagnetic induction data*, Surv. Geophys., 35 (2014), pp. 85–100.
- [49] S. REITZINGER, U. SCHREIBER, AND U. VAN RIENEN, *Algebraic multigrid for complex symmetric matrices and applications*, J. Comput. Appl. Math., 155 (2003), pp. 405–421.
- [50] Y. SAAD, *Iterative Methods for Sparse Linear Systems*, SIAM, Philadelphia, PA, 2003.
- [51] H. Si, *Tetgen: A Quality Tetrahedral Mesh Generator and Three-Dimensional Delaunay Triangulator*, <http://tetgen.berlios.de>, 2007.
- [52] H. Si, *TetGen, a delaunay-based quality tetrahedral mesh generator*, ACM Trans. Math. Softw., 41 (2015), pp. 11:1–11:36, <https://doi.org/10.1145/2629697>, <http://doi.acm.org/10.1145/2629697>.
- [53] B. SIEMON, A. V. CHRISTIANSEN, AND E. AUKEN, *A review of helicopter-borne electromagnetic methods for groundwater exploration*, Near Surface Geophys., 7 (2009), pp. 629–646, <https://doi.org/10.3997/1873-0604.2009043>.
- [54] R. SMITH, *Electromagnetic induction methods in mining geophysics from 2008 to 2012*, Surv. Geophys., 35 (2014), pp. 123–156.
- [55] R. STREICH, *Controlled-source electromagnetic approaches for hydrocarbon exploration and monitoring on land*, Surv. Geophys., 37 (2016), pp. 47–80.
- [56] P. W. WALKER AND G. F. WEST, *A robust integral equation solution for electromagnetic scattering by a thin plate in conductive media*, Geophysics, 56 (1991), pp. 1140–1152.